Respiratory Motion Modeling and Estimation

Tobias Klinder[1,2], Cristian Lorenz[2], and
Jörn Ostermann[1]

[1] Institut für Informationsverarbeitung, Leibniz University of Hannover, Germany,
klinder@tnt.uni-hannover.de,
[2] Philips Research Europe - Hamburg, Sector Medical Imaging Systems, Germany *

Abstract. In order to cope with the problems caused by breathing motion, it would be beneficial for many applications to incorporate prior knowledge of respiratory motion. In this paper, we present the extraction, modeling, and prediction of respiratory motion based on inhale-exhale pairs of CT images. Intra- and inter-patient motion models of the lungs are built and adapted to unseen data by the use of sparse motion indicators. The created models are thereby represented as a linear model by applying Principal Component Analysis (PCA) on the covariance of motion vectors of corresponding landmarks. For model adaptation, diaphragm and rib-cage are investigated as model stimulators and compared to a systematical selection of landmarks holding most of the model's variability. While the diaphragm motion correlates well with the breathing motion achieving an average estimation error of 3.0 mm for the intra- and 4.1 mm for the inter-patient models in average, the predictability of breathing based on the rib-cage motion is significantly worse. Using both diaphragm and rib-cage as stimulators, we obtained an average estimation error of 2.8 mm for the intra- and 3.7 mm for the inter-patient models improving prediction.

1 Introduction

Respiratory motion is a key issue in radiation therapy, tumor ablation, and other treatments of the thorax and upper abdomen [1] but also for data acquisition. Since breathing motion causes a significant organ movement and deformation, an accurate knowledge of the localisation of the object in focus is difficult to obtain. However, a precise prediction of the structures of interest would be highly desirable for many applications, e.g., for dose reduction of healthy tissue during radiotherapy treatment. One approach to reduce the uncertainties caused by breathing is to use prior knowledge of the respiratory motion as, e.g., in the form of breathing models. In contrast to biomechanical models [2, 3] that aim a physically-based modeling of the lung, our goal is to build a general breathing model from an ensemble of motion fields extracted, e.g., from 4D-CT or 4D-MR, and individualize this general model using sparse motion indicators to obtain a dense motion field for the organ under investigation.

* We thank K. Franks, J.P. Bissonette, T. Purdie, and A. Bezjak, Radiation Medicine Program, Princess Margaret Hospital, Toronto, Canada for all image data.

Little work has been presented for building motion models based on extracted motion fields from 4D image data while not considering tissue properties. Admittedly, in many cases the generated models were patient-specific, e.g., [4, 5], which means that in a clinical scenario, motion information can only be incorporated if images of the patient are already available or additionally acquired. In contrast to patient-specific approaches, Sundaram et al. [6] created a dynamic model of average lung deformation also registering between subjects. However, the method did not address the clinically relevant case of adapting a learned general model to a certain patient. Motion model adaptation of an inter-subject model by the use of sparse motion information has been recently presented for liver deformation to predict the drift of the exhalation position of corresponding points inside the liver [7].

In this paper, we address the problem of extracting, modeling and estimating breathing motion based on inhale-exhale pairs of CT images. We do not only deal with intra-patient model building as well as its adaptation to estimate breathing motion on different days throughout treatment, but also build inter-subject models to predict patient-specific motion learned from a general model.

Section 2.1 introduces the available image data. Based on the motion field extraction introduced in Sect. 2.2, motion model building is explained in Sect. 2.3. The adaptation of our motion models to unseen data based on sparse motion indicators is presented in Sect. 2.4. Systematic selection of regions providing sparse motion information is explained in Sect. 2.5. Finally, performance of our motion models is presented in Sect. 3.

2 Methods

2.1 Image Data

Inhale and exhale thorax CT images of seven patients all suffering from lung cancer were available over several weeks of treatment during radiotherapy. For each patient, image data of up to seven weeks plus two weeks of preliminary examination was acquired. Thus, this image data captures the variability in breathing motion throughout different weeks of treatment. Due to the fact that all images where acquired at breath hold, motion artifacts caused by breathing were not present. All images had an in-plane resolution of 0.85-0.97 mm and a slice thickness of 2.5 mm. Since the images were acquired for radiotherapy planning where the focus was set on the trajectory of the tumor, not all cases show the lungs entirely. These cases were removed from further investigation.

2.2 Motion Field Extraction

Lung motion fields are derived from inhale-exhale images using a surface-based tracking technique where the surface is represented as a triangulated mesh. By propagating a topologically identical patient-specific lung surface mesh from inhale to exhale, anatomical point correspondences are assumed to be preserved.

The trajectories of corresponding points of the adapted meshes thus provide a sparse motion field. A continuous description of the sparse motion field is finally obtained by interpolation using thin-plate-splines [8]. For the extraction of motion fields from 4D-CT data an abundant amount of other methods exist. In [9], we have recently compared surface-based tracking to three other common techniques. Mesh propagation extracts motion fields that provide an accuracy to manually set landmarks of approximately the voxel size. In a qualitative analysis, the motion fields show plausible characteristics also similar to the other methods. Most prominent advantages of surface-tracking are its ability to cope with discontinuities in motion fields, its low computational cost, and the fact that it directly provides a segmentation in all phases.

Patient-specific lung surface models for motion field extraction are obtained by selecting one chosen reference inhale image per patient and apply a triangulation of the thresholded image. These meshes cover the outer border of the lung lobes and also the surfaces of the bronchial and pulmonary vessel tree as well as the tumor surfaces [8]. By adapting the generated patient-specific reference lung mesh to inhale and exhale images over all weeks of treatment, vertex correspondences are preserved for all images of the same patient.

In addition to the lung motion field, the movement of the rib-cage is extracted. For that purpose, a general rib-cage surface model [10] is automatically positioned in all inhale images, adapted, and finally propagated to the corresponding exhale image. Since all ribs and vertebrae are labeled separately, motion fields can be easily assigned to each individual structure.

For both lung and rib-cage, mesh adaptation is performed using an iterative shape-constrained deformable surface model method [11]. In each iteration, the concordance of model and object boundary in the image is optimized. An appropriate parameter setting for lung surface mesh propagation can be found in [8]. Figure 1 shows the adapted surface meshes of lung and rib-cage in one data set.

2.3 Motion Modeling

The proposed motion models capture the variability in motion of a given learning set by applying principal component analysis (PCA) on the covariance matrix of the motion fields. Since the key issue for model building is to establish corresponding landmarks, this aspect will be explained separately for intra- and inter-patient motion models in detail below.

Suppose we have a set of M **motion fields** denoted as $\mathbf{v}_1, \ldots, \mathbf{v}_M$. Each $\mathbf{v}_i$ contains the components of N **motion vectors** $\mathbf{a}_j$ defined at N corresponding landmark positions $\mathbf{v}_i = [a_{1i_x}, a_{1i_y}, a_{1i_z}, \ldots, a_{Ni_x}, a_{Ni_y}, a_{Ni_z}]^T$. After aligning our training sets, averaging all vectors, and applying PCA on the covariance matrix, we obtain a mean motion field $\bar{\mathbf{v}}$ and its principal modes of variation ϕ_k covered in the matrix $\mathbf{\Phi}$. Thus, we can express a given motion field $\mathbf{v}_i$ as

$$\mathbf{v}_i = \bar{\mathbf{v}} + \mathbf{\Phi}\mathbf{b}_i \tag{1}$$

where $\mathbf{b}_i$ is the weight vector.

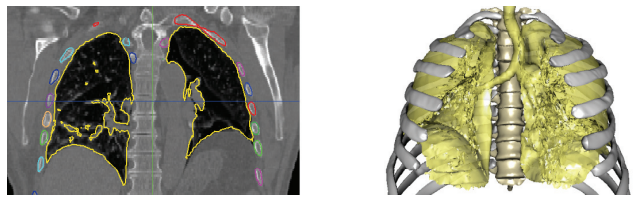

Fig. 1. Extracted lung surface mesh and adapted rib-cage shown in one slice and as surface rendering. Coloring in image slice indicates labeling of individual structures.

Intra Patient Since a topologically identical mesh is adapted to all images of the same patient as explained in Sect. 2.2, corresponding vertices are assumed to provide the correspondences of our intra-patient motion model.
Inter Patient Motion field extraction was based on patient specific surface meshes. Thus, vertex correspondences between meshes of different patients were not given. In order to establish inter-subject correspondences, a model of the outer surfaces of the lung [12] is additionally adapted to all data sets. By adapting a topologically identical surface model, we again assume anatomical point correspondences to be preserved. However, in order to not only establish correspondences on the outer surface of the lung but also in the inside, we moreover define a cartesian grid inside the lung mesh. A patient-specific grid inside the lung is obtained by applying a thin-plate spline deformation field calculated from corresponding points of individualized surface and lung model to the grid points. Figure 2 illustrates the definition of inter-subject correspondences.

In case of the rib-cage, corresponding landmarks are obtained for both intra- and inter-patient models from corresponding mesh vertices since the same model was adapted to all patients.

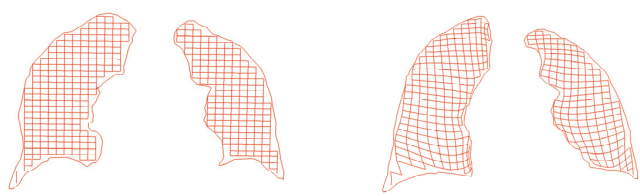

(a) Reference grid of lung model (b) Patient individualized grid

Fig. 2. Establishing inter-patient correspondences. Reference cartesian is deformed by calculated thin-plate spline deformation field which uses corresponding vertices of the outer lung surfaces. Examplarily, warping is shown for two-dimensional contour.

2.4 Motion Model Adaptation

The task of estimating the patient's motion field $\mathbf{v}$ under the assumption of sparse motion indicators expressed as $\mathbf{v}_b$ can be modeled as a conditional distribution $p(\mathbf{v}_a|\mathbf{v}_b)$ where $\mathbf{v}_a$ are the motion vectors of the vertices to be estimated. We are interested in the maximum likelihood estimation of the conditional distribution under the condition that the motion of a small set of landmarks is known. For that purpose, we partition the motion field $\mathbf{v}$ into to two disjoint subsets $\mathbf{v}_a$ and $\mathbf{v}_b$ resulting in

$$\mathbf{v} = \begin{pmatrix} \mathbf{v}_a \\ \mathbf{v}_b \end{pmatrix} \tag{2}$$

and equivalent partitions for the mean vector $\bar{\mathbf{v}}$ and the covariance matrix $\mathbf{\Sigma}$

$$\bar{\mathbf{v}} = \begin{pmatrix} \bar{\mathbf{v}}_a \\ \bar{\mathbf{v}}_b \end{pmatrix} \qquad \mathbf{\Sigma} = \begin{pmatrix} \mathbf{\Sigma}_{aa} & \mathbf{\Sigma}_{ab} \\ \mathbf{\Sigma}_{ba} & \mathbf{\Sigma}_{bb} \end{pmatrix} . \tag{3}$$

The maximum likelihood estimate $\bar{\mathbf{v}}_{a|b}$ of the conditional distribution given $\mathbf{v}_b$ can be calculated as [13]

$$\bar{\mathbf{v}}_{a|b} = \bar{\mathbf{v}}_a + \mathbf{\Sigma}_{ab}\mathbf{\Sigma}_{bb}^{-1}(\mathbf{v}_b - \bar{\mathbf{v}}_b) . \tag{4}$$

Note that usually, $\mathbf{\Sigma}_{bb}^{-1}$ is not invertible owing to multi-collinearity in the landmark positions and unreliable due to chance covariance in a limited training set. Therefore, we apply some regularization. In this case, we perform a ridge regression [14] by replacing $\mathbf{\Sigma}_{bb}^{-1}$ with $\hat{\mathbf{\Sigma}}_{bb}^{-1} = \mathbf{\Sigma}_{bb}^{-1} + \gamma\mathbf{I}$, where γ is a positive and typically small constant.

2.5 Landmark Selection

For many clinical applications, an indication of optimal positions for sparse motion indicators is of special interest, e.g., in case of MRI navigator images. Assume that we were able to place motion indicators at arbitrary positions inside the lung neglecting any practical limitations. Then the question arises what will be the optimal choice for indicator positions? We tackle the problem in an iterative procedure using the properties of our created motion model. In order to find positions with most predictive power, we try out any motion vector as motion predictor and select the corresponding landmark position that belongs to the motion vector which reduces the variance of the model more than others. After calculating the modes invariant with respect to that chosen motion vector, we rerun the selection.

For the pointwise selection, we follow the formulation given in [15], where the variability of the weight vectors $\mathbf{b}_i$ before and after creating the invariant modes are compared.

Assuming the same partioning into two disjoint subsets as derived for the mean and covariance in Eq. 3 also for the corresponding matrix $\mathbf{\Phi}$ containing

the eigenvectors, we obtain:

$$\mathbf{\Sigma} = \mathbf{\Phi}\mathbf{D}\mathbf{\Phi}^T = \begin{pmatrix} \mathbf{\Phi}_a\mathbf{D}\mathbf{\Phi}_a^T & \mathbf{\Phi}_a\mathbf{D}\mathbf{\Phi}_b^T \\ \mathbf{\Phi}_b\mathbf{D}\mathbf{\Phi}_a^T & \mathbf{\Phi}_b\mathbf{D}\mathbf{\Phi}_b^T \end{pmatrix} \quad \text{with} \quad \mathbf{\Phi} = \begin{pmatrix} \mathbf{\Phi}_a \\ \mathbf{\Phi}_b \end{pmatrix} . \tag{5}$$

The diagonal matrix of eigenvalues is denoted as $\mathbf{D}$.

Following [15], we express the invariant mode $\hat{\mathbf{b}}_i$ by

$$\hat{\mathbf{b}}_i = \mathbf{b}_i - \mathbf{R}_b\mathbf{\Phi}_b\mathbf{b}_i = (\mathbf{I} - \mathbf{R}_b\mathbf{\Phi}_b)\mathbf{b}_i \,, \tag{6}$$

with $\mathbf{R}_b = \mathbf{D}\mathbf{\Phi}_b^T[\mathbf{\Phi}_b\mathbf{D}\mathbf{\Phi}_b^T]^{-1}$.

Comparing the variability of the weight vectors before and after creating the invariant mode with respect to the stimulator expressed as $\mathbf{v}_b$, the points with maximal predictive power can be found. Note that in this case $\mathbf{v}_b$ contains the motion vector corresponding to one landmark position. When applying this procedure iteratively, the k best predictors can be found.

3 Results

As shown in [9], the motion fields extracted as in Sect. 2.2 provide a landmark accuracy of about the voxel size. Thus, for the following evaluation of our motion models, we assume the extracted motion fields as our ground truth. While this enables us to evaluate the performance of our models at a few thousand discrete positions meaning the mesh vertices, it has to be noted that there might be a slight bias compared to landmarks set by experts.

For evaluation of our motion models, we are interested in the possibility to predict inhale-exhale motion fields of the lungs. We compare the prediction of anatomical related regions to systematic landmark selection from Sect. 2.5. In each case prediction is performed as described in Sect. 2.4. As anatomical related regions, we focus on the main breathing motors which are diaphragm and rib-cage. The diaphragm motion is extracted by manually labelling the dome of the surfaces close to the diaphragm on all lung models. As stimulators for model adaptation as described in Sect. 2.4, we then use all motion vectors belonging to the vertices of the labelled surfaces. In case of the rib-cage, we focus on the rib motion since there is almost no spine motion.

Intra patient motion models are evaluated in a leave-one-out study. In each case, one week is chosen and a motion model is built out of all remaining weeks and adapted to the 'unseen' motion field. The estimated motion field is then compared to the respective extracted motion field and the error at mesh vertices is evaluated. The results when using diaphragm and rib-cage as model stimulators are given in Tab. 1. By comparing the prediction power of the respective anatomical region to the mean motion model $\bar{\mathbf{v}}$, it can be seen that model stimulation using the diaphragm denoted as PCA_{DIA} significantly improves the estimation while the rib-cage (PCA_{RC}) even worsens the prediction. However, using both diaphragm and rib motion (PCA_{RCD}) as model stimulators yields almost the optimal parameter fit with an error of 2.8 mm in average. The best

possible prediction that can be achieved with our model is given for comparison by projecting the true motion field in the PCA space. Figure 3 shows the prediction in the sagittal view for two selected cases.

Inter patient motion models are evaluated in a similar leave-one-out study. Motion models of all patients besides the one under consideration are built and adapted to all weeks of the corresponding patient with results given in Tab. 1. Although we observed significant differences in breathing patterns between patients, there have to be similarities in the respective motion fields which can be seen from the fact that the mean model already compensates about 40 % of the breathing motion. In case of the inter-patient model, we took into account 20 eigenvectors that correspond to the largest eigenvalues covering about 98% of the variance. Again, the prediction using the diaphragm is much better than using the rib-cage with 4.1 mm in average compared to 7.4 mm.

When applying landmark selection from Sect. 2.5 on both intra- and inter-patient models, the predictive power of the first N-landmarks was investigated. In each case, we additionally took all neighboring vertices into account to be less sensitive to the exact landmark position. Having motion information only at the positions of the first N=3 selected landmarks including their neighbors yields an error of 4.0 (5.8) mm in average for intra-(inter-) patient models and for N=5 and N=7 an error of 3.5 (5.1) mm and 3.0 (4.8) mm, respectively. A typical distribution for N=5 is given in Fig. 4. For many cases, it could be observed that the first selected landmark was located close to the diaphragm while the second one in the anterior part of the corresponding other upper lung.

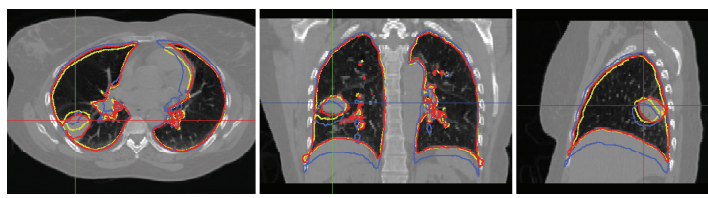

Fig. 3. Result of motion estimation shown in three orthogonal slices for Patient 3 using the inter-subject motion model and assuming the motion of the dome of the diaphragm to be known. Inhale contour is shown blue, red exhale, and yellow estimation.

4 Conclusion

Breathing motion is a complicated factor in several applications working on the thorax or upper abdomen. In many cases, the treatment would benefit from prior knowledge of the organ deformation and location. Although latest image devices are able to acquire dynamic images covering the respiratory motion, e.g.,

Table 1. Result of intra- and inter-patient motion models. Approximation of inhale-exhale motion by model in leave-one-out test. All values are given in millimeters. Performance of mean motion model as well as PCA model with optimal parameter fit indicates model quality. Prediction error is given when using different model stimulators. Mean motion of entire lung and respective regions presented for comparison ($\mathbf{m}$, $\mathbf{m}_{DIA}$, $\mathbf{m}_{RC}$). Last row gives mean value of all rows as absolute value and relative to mean lung motion in percent. For details see text.

Intra Patient Model								
	$\bar{\mathbf{v}}$	PCA	PCA_{DIA}	PCA_{RC}	PCA_{RCD}	$\tilde{\mathbf{m}}$	$\tilde{\mathbf{m}}_{DIA}$	$\tilde{\mathbf{m}}_{RC}$
Pat. 1	4.1 ± 1.2	2.1 ± 0.7	2.3 ± 0.7	4.8 ± 1.9	2.2 ± 0.7	10.9 ± 1.7	15.4	3.7
Pat. 2	4.5 ± 1.4	2.8 ± 0.9	4.1 ± 1.3	4.9 ± 1.6	3.2 ± 0.9	12.6 ± 2.4	23.1	9.7
Pat. 3	2.2 ± 0.5	1.4 ± 0.3	1.5 ± 0.4	2.0 ± 0.5	1.5 ± 0.4	6.9 ± 1.5	12.0	2.4
Pat. 4	4.6 ± 1.9	1.7 ± 0.5	1.9 ± 0.6	3.3 ± 1.5	2.0 ± 0.4	10.0 ± 4.1	20.9	3.4
Pat. 5	4.7 ± 1.5	3.3 ± 0.7	4.0 ± 0.7	4.9 ± 1.3	3.9 ± 0.6	7.3 ± 2.2	11.1	4.6
Pat. 6	4.2 ± 0.6	3.8 ± 0.8	4.2 ± 1.2	4.8 ± 0.5	3.9 ± 1.0	10.8 ± 2.1	20.2	3.2
Pat. 7	3.2 ± 0.7	3.0 ± 0.8	3.3 ± 1.0	3.4 ± 1.4	3.1 ± 1.1	10.0 ± 1.4	18.7	4.1
mean	3.9 (39.8)	2.6 (26.4)	3.0 (30.6)	4.0 (40.1)	2.8 (28.9)	9.8	17.3	4.4

Inter Patient Model								
	$\bar{\mathbf{v}}$	PCA	PCA_{DIA}	PCA_{RC}	PCA_{RCD}	$\tilde{\mathbf{m}}$	$\tilde{\mathbf{m}}_{DIA}$	$\tilde{\mathbf{m}}_{RC}$
Pat. 1	6.3 ± 1.2	3.2 ± 0.5	4.1 ± 0.8	7.0 ± 1.6	4.1 ± 0.8	10.9 ± 1.7	15.4	3.7
Pat. 2	8.6 ± 1.8	4.3 ± 0.6	6.1 ± 1.0	11.0 ± 3.0	5.0 ± 0.9	12.6 ± 2.4	23.1	9.7
Pat. 3	3.6 ± 0.4	1.8 ± 0.1	2.7 ± 0.3	5.0 ± 1.0	2.1 ± 0.3	6.9 ± 1.5	12.0	2.4
Pat. 4	6.7 ± 1.8	2.8 ± 0.7	3.9 ± 1.0	6.6 ± 2.4	3.6 ± 1.0	10.0 ± 4.1	20.9	3.4
Pat. 5	5.9 ± 1.6	2.5 ± 0.4	3.1 ± 0.4	7.4 ± 0.8	3.2 ± 0.5	7.3 ± 2.2	11.1	4.6
Pat. 6	8.0 ± 1.2	4.0 ± 1.0	4.8 ± 1.0	9.0 ± 2.3	4.6 ± 1.0	10.8 ± 2.1	20.2	3.2
Pat. 7	4.3 ± 1.0	2.9 ± 0.4	4.1 ± 0.5	6.0 ± 0.7	3.6 ± 0.6	10.0 ± 1.4	18.7	4.1
mean	6.2 (63.3)	3.1 (31.6)	4.1 (41.9)	7.4 (75.8)	3.7 (37.7)	9.8	17.3	4.4

4D-CT, there is not always a multiphase breathing gated examination available. Thus, in this paper, we focused on motion model creation from inhale-exhale pairs of CT data sets and adaptation to 'unseen' data. Due to the fact that the images were acquired at breath-hold, no image artifacts caused by breathing were present. From the extracted motion fields, patient-specific models but also inter-subject models have been built and compared. For model stimulation, different sparse motion indicators have been investigated. If the diaphragm motion is known, we achieved a prediction error of 3.0 (4.1) mm for the intra (inter)-patient model covered. Using sparse motion information obtained from the rib-cage is thereby less appropriate. With a systematic selection of landmarks, most important regions for providing sparse motion information have been found. Although there are several attempts for patient-specific modeling, it is to the best of our knowledge the first time that an inter-subject breathing model based on statistical properties of extract motion fields has been built and adapted to patient data.

Since we worked so far on a small size of training data, improvement can probably be expected when enlarging the amount of patient data. Future studies will be carried out on multiphase data taking the dynamic properties of respiration into account.

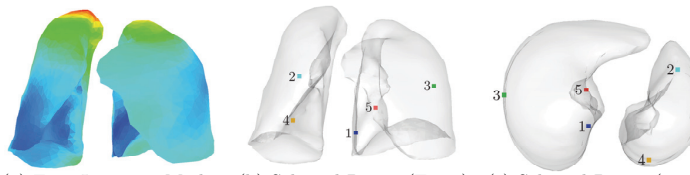

(a) First Invariant Mode (b) Selected Points (Front) (c) Selected Points (Top)

Fig. 4. Systematic point selection. Potential predictive power of each landmark position displayed on mesh surface (a). Ratio of variance of coefficients $\hat{\mathbf{b}}_i$ and $\mathbf{b}_i$ from Eq. 6 color coded from blue (small) to red (high). Selected first five points color coded from first (blue) to fifth (red) shown in (b) and (c). First selected point typically close to diaphragm while second in corresponding other lung.

References

1. Balter, J.M., ten Haken, R.K., Lawrence, T.S., Lam, K.L., Robertson, J.M.: Uncertainties in CT-based radiation therapy treatment planning associated with patient breathing. International Journal on Radiation Oncology, Biology, Physics **36**(1) (1996) 167–174
2. Villard, P.F., Beuve, M., Shariat, B., Baudet, V., Jaillet, F.: Simulation of lung behaviour with finite elements: Influence of bio-mechanical parameters. In: Proc. MEDIVIS. (2005) 9–14
3. Werner, R., Ehrhardt, J., Schmidt, R., Handels, H.: Modeling respiratory lung motion: a biophysical approach using finite element methods. In: Proc. SPIE. Volume 6916. (2008) 69160N1–11
4. McClelland, J.R., Blackall, J.M., Tarte, S., et al.: A continuous 4D motion model from multiple respiratory cycles for use in lung radiotherapy. Medical Physics **33**(9) (2006) 3348–3358
5. Zhang, Q., Pevsner, A., Hertanto, A., Hu, Y.C., Rosenzweig, K.E., Ling, C.C., Mageras, G.S.: A patient-specific respiratory model of anatomical motion for radiation treatment planning. Medical Physics **34**(12) (2007) 4772–4782
6. Sundaram, T.A., Avants, B.B., Gee, J.C.: A dynamic model of average lung deformation using capacity-based reparameterization and shape averaging of lung mr images. In: Proc. MICCAI. Volume 3217. (2004) 1000–1007
7. von Siebenthal, M., Szkely, G., Lomax, A., Cattin, P.: Inter-subject modelling of liver deformation during radiation therapy. In: Proc. MICCAI. Volume 4791. (2007) 659–666

8. Klinder, T., Lorenz, C., von Berg, J., Renisch, S., Blaffert, T., Ostermann, J.: 4DCT image-based lung motion field extraction and analysis. In: Proc. SPIE Medical Imaging. Volume 6914. (2008) 69141L1–11
9. Vik, T., Kabus, S., von Berg, J., Ens, K., Dries, S., Klinder, T., Lorenz, C.: Validation and comparison of registration methods for free-breathing 4d lung-ct. In: Proc. SPIE Medical Imaging. Volume 6914. (2008) 69142P1–10
10. Klinder, T., Lorenz, C., von Berg, J., Dries, S., Blow, T., Ostermann, J.: Automated model-based rib cage segmentation and labeling in CT images. In: Proc. MICCAI. Volume 4792. (2007) 195–203
11. Weese, J., Kaus, M., Lorenz, C., et al.: Shape constrained deformable models for 3D medical image segmentation. In: Proc. IPMI. (2001) 380–387
12. Blaffert, T., Barschdorf, H., von Berg, J., Dries, S., et al.: Lung lobe modeling and segmentation with individualized surface meshes. In: Proc. SPIE Medical Imaging. Volume 6914. (2008) 69141I1–10
13. Bishop, C.M.: Pattern Recognition and Machine Learning. Springer (2006)
14. Hoerl, A., Kennard, R.: Ridge regression: Biased estimation for nonorthogonal problems. Technometrics **12**(1) (1970) 5567
15. Hug, J., Brechbühler, C., Szekely, G.: Model-based initialisation for segmentation. In: Proc. ECCV. Volume 1843. (2000) 290–306